

AEOS: The Impact of Pop III Initial Mass Function and Star-by-Star Models in Galaxy Simulations

KALEY BRAUER,¹ JENNIFER MEAD,² JOHN H. WISE,³ GREG L. BRYAN,² MORDECAI-MARK MAC LOW,^{4,2} ALEXANDER P. JI,^{5,6}
ANDREW EMERICK,⁷ ERIC P. ANDERSSON,⁴ ANNA FREBEL,⁸ AND BENOIT CÔTE^{9,10}

¹*Center for Astrophysics | Harvard & Smithsonian, Cambridge, MA 02138, USA*

²*Department of Astronomy, Columbia University, New York, NY 10027, USA*

³*Center for Relativistic Astrophysics, School of Physics, Georgia Institute of Technology, Atlanta, GA 30332, USA*

⁴*Department of Astrophysics, American Museum of Natural History, New York, NY 10024, USA*

⁵*Department of Astronomy & Astrophysics, University of Chicago, 5640 S Ellis Avenue, Chicago, IL 60637, USA*

⁶*Kavli Institute for Cosmological Physics, University of Chicago, Chicago, IL 60637, USA*

⁷*Carnegie Observatories, Pasadena, CA, 91101, USA*

⁸*Department of Physics and Kavli Institute for Astrophysics and Space Research, Massachusetts Institute of Technology, Cambridge, MA 02139, USA*

⁹*Department of Physics and Astronomy, University of Victoria, Victoria, BC, V8P5C2, Canada*

¹⁰*Konkoly Observatory, Research Centre for Astronomy and Earth Sciences, HUN-REN, Konkoly Thege M. ut 15-17, Budapest 1121, Hungary*

ABSTRACT

We explore the effect of variations in the Population III (Pop III) initial mass function (IMF) and star-by-star feedback on early galaxy formation and evolution using the AEOS simulations. We compare simulations with two different Pop III IMFs: $M_{\text{char}} = 10M_{\odot}$ and $M_{\text{max}} = 100M_{\odot}$ (Aeos10) and $M_{\text{char}} = 20M_{\odot}$ and $M_{\text{max}} = 300M_{\odot}$ (Aeos20). Aeos20 produces significantly more ionizing photons, ionizing 30% of the simulation volume by $z \approx 14$, compared to 9% in Aeos10. This enhanced ionization suppresses galaxy formation on the smallest scales. Differences in Pop III IMF also affect chemical enrichment. Aeos20 produces Population II (Pop II) stars with higher abundances, relative to iron, of light and α -elements, a stronger odd-even effect, and a higher frequency of carbon-enhanced metal-poor stars. The abundance scatter between different Pop II galaxies dominates the differences due to Pop III IMF, though, implying a need for a larger sample of Pop II stars to interpret the impact of Pop III IMF on early chemical evolution. We also compare the AEOS simulations to traditional simulations that use single stellar population particles. We find that star-by-star modeling produces a steeper mass-metallicity relation due to less bursty feedback. These results highlight the strong influence of the Pop III IMF on early galaxy formation and chemical evolution, emphasizing the need to account for IMF uncertainties in simulations and the importance of metal-poor Pop II stellar chemical abundances when studying the first stars.

Keywords: Population III stars – Chemical enrichment – Dwarf galaxies – Ionization

1. INTRODUCTION

The formation of the first stars, known as Population III (Pop III), marked a pivotal transition in the evolution of the early Universe (Klessen & Glover 2023; Barkana & Loeb 2001; Bromm 2013; Bromm et al. 2002; Wise & Abel 2008). Composed solely of primordial gas, these stars drove the chemical enrichment of the first galaxies. A key factor in determining the properties of these nascent galaxies is the initial mass function (IMF) of the Pop III stars (e.g., Schaerer

2002; Schneider et al. 2006; Hartwig et al. 2015; Stacy et al. 2016; Ishigaki et al. 2018; Lazar & Bromm 2022; Parsons et al. 2022). Understanding the Pop III IMF is crucial for constraining the feedback mechanisms that regulated star formation and the transition to later populations of stars.

Early numerical simulations suggested that the Pop III IMF was top-heavy, favoring very massive stars reaching hundreds or even a thousand solar masses (Abel et al. 2002; Bromm et al. 2002). This result stemmed from the inability of the primordial gas to cool efficiently, leading to the formation of large single stars. However, more recent high-resolution simulations have suggested that gas cloud fragmentation could produce a broader range of stellar masses, extending down to tens of solar masses or even lower

(Hosokawa et al. 2011; Hirano et al. 2014; Susa et al. 2014; Stacy et al. 2016). These results suggest that the Pop III IMF (which is still distinct from a classical Pop II IMF) encompasses a broad range of stellar masses, allowing for the formation of both extremely massive and relatively lower-mass stars in the early universe.

Indirect observational evidence further supports the idea of a broad Pop III IMF. Metal-poor stars observed in the Milky Way and its satellite galaxies retain chemical abundance patterns that may represent enrichment by Pop III stars (Hartwig et al. 2018). When these patterns are compared to theoretical models of Pop III supernova yields, they can offer insights into the masses of Pop III progenitors. Some data suggest that certain enriched stars originated from Pop III progenitors with masses exceeding $50 M_{\odot}$ (Ji et al. 2024) and even up to $260 M_{\odot}$ (Xing et al. 2023); however, the latter finding is contested by recent work (Skúladóttir et al. 2024). Meanwhile, the majority of Pop III progenitors may have had masses of only a few tens of solar masses (Ishigaki et al. 2018; Fraser et al. 2017; Tumlinson 2006). While some models propose a Salpeter-like IMF to describe the Pop III mass distribution, recent studies have pointed to possible deviations from this power law, including a potential peak around $25 M_{\odot}$ (Ishigaki et al. 2018). The non-detection of zero-metallicity stars in ultra-faint dwarf galaxies also provides constraints on the minimum mass of the first stars, $M_{\min} > 0.8 M_{\odot}$ (Rossi et al. 2021).

Despite these advances, significant uncertainties remain regarding the true shape of the Pop III IMF and its implications for galaxy formation and reionization. Simulations provide a valuable tool for exploring these uncertainties by modeling different IMF scenarios and examining their effects on key cosmic processes. The amount of ionizing radiation produced by Pop III stars, for instance, depends heavily on their mass distribution, directly impacting the ionization history of the universe and star formation in early galaxies (Schaefer 2002; Wise et al. 2012a; Kimm et al. 2017). Likewise, stellar feedback from SNe and winds influences the growth and chemical evolution of the earliest galaxies (Wise et al. 2012b; Heger & Woosley 2010).

The legacy of the Pop III stars extends to the formation of Population II (Pop II) stars (e.g., Prgomet et al. 2022). The Pop III IMF influences the characteristics of the Pop II stars, which emerged after the interstellar medium was enriched by metals from Pop III SNe. Massive Pop II stars play a critical role in early galaxy evolution as they contribute significantly to the regulation of star formation through feedback processes such as ionizing radiation, stellar winds, and SNe (Somerville & Davé 2015). These feedback mechanisms drive gas outflows, influence the ionization history, and regulate the growth of early galaxies. Accurately capturing the effects of individual Pop II stars on their environment is

therefore also essential for understanding the formation and evolution of the first galaxies (e.g., Brauer et al. 2025; Andersson et al. 2025).

Traditional cosmological simulations often simplify the modeling of Pop II stellar feedback by representing entire star clusters as single particles, which limits the resolution of the feedback processes that individual stars provide (e.g., Skinner & Wise 2020; Smith 2021). Such models can overlook the detailed radiative and mechanical feedback from individual stars, which plays a critical role in regulating the interstellar medium and shaping galaxy evolution. In recent years, simulations have begun to include feedback from individual stars in galaxy simulations (e.g., Emerick et al. 2019; Lahén et al. 2020; Hirai et al. 2021; Gutcke et al. 2021; Hislop et al. 2022; Andersson et al. 2023; Calura et al. 2022; Steinwandel et al. 2023; Brauer et al. 2025; Hirai et al. 2024; Deng et al. 2024). Star-by-star modeling of Pop II stellar feedback offers a more detailed approach. This captures the impact of the radiation, supernovae (SNe), and stellar winds from individual stars both inside and outside clusters on gas dynamics and chemical enrichment, which is crucial for understanding the earliest stages of galaxy formation.

In this work, we present results from the AEOS simulations (Brauer et al. 2025; Mead et al. 2025) that explore (1) the impact of varying the Pop III IMF on early galaxy evolution and (2) the impact of star-by-star models when simulating the first galaxies. These AEOS simulations model the formation of the first stars and galaxies in the first few hundred megayears of the universe, following individual stellar feedback and detailed chemical enrichment. This approach is motivated by the fundamental importance of predicting the chemical abundances of ancient stars, particularly those found in ultra-faint dwarf galaxies and the Milky Way’s stellar halo, to unravel the processes of early star and galaxy formation (e.g., Brauer et al. 2019).

In Section 2, we summarize our methodology, describe our simulations, and detail how they differ. In Section 3, we compare two individual star simulations that differ only in their Pop III IMFs. These simulations allow us to investigate how changes in the IMF affect star formation rates, galaxy growth, ionization history, and metal enrichment. In Section 4, we compare one of the simulations to seven comparison simulations without star-by-star feedback to investigate the effect of highly resolved star formation and feedback on galaxy evolution. We conclude in Section 5.

2. METHODS

This study uses the numerical methods detailed in Brauer et al. (2025). We focus on a comparative analysis between the fiducial AEOS cosmological simulation and additional simulations: (1) an AEOS simulation with an altered Pop III IMF with a higher characteristic mass M_{char} and upper mass cut-

off, and (2) seven comparison simulations that omit the full star-by-star feedback and enrichment models, instead using single stellar population particles and IMF averaged metal yields. The comparison simulations are identical except for stochastic differences to show how stochasticity affects results. Below, we provide a concise summary of the important methods from Brauer et al. (2025) and elaborate on the modifications pertinent to the additional simulations. The differences in the simulations are summarized in Table 1.

2.1. Similarities Across Simulations

All simulations use the ENZO adaptive mesh refinement (AMR) code (Bryan et al. 2014; Brummel-Smith et al. 2019), enabling high-resolution modeling of cosmological structures. The computational grid employs AMR to achieve high physical resolution in regions of elevated gas density, ensuring detailed resolution of dense gas clumps and star formation. They have a root-grid resolution of 256^3 , a dark matter resolution of $1840 M_\odot$, and a resolution of 1 physical pc at the finest scales.

The simulations cover a comoving $(1 \text{ Mpc})^3$ volume, simulated from redshift $z = 130$ to $z = 14.5$, approximately 300 Myr after the Big Bang. They commence from identical initial conditions generated with MUSIC (Hahn & Abel 2011) at redshift $z = 130$, adhering to the cosmological parameters derived from the Planck collaboration (Planck Collaboration et al. 2014). This ensures consistency across all simulation runs, facilitating comparisons between different feedback models and IMF choices.

Star formation is modeled stochastically in cold, dense gas regions with $n > 10^4 \text{ cm}^{-3}$ that exhibit converging flows having $\nabla \cdot \mathbf{v} < 0$, assuming a star formation efficiency per free-fall time of $e_{\text{ff}} = 2\%$. The star formation algorithm distinguishes Pop II from Pop III stars using a threshold of total gas metallicity $Z > 10^{-5} Z_\odot$ (Ji et al. 2014; Chiaki et al. 2015; Schneider et al. 2012; Tumlinson 2006). Pop III star formation in lower metallicity gas further requires a molecular hydrogen fraction $f_{\text{H}_2} > 0.005$, consistent with high-resolution simulations (Susa et al. 2014; Kulkarni et al. 2021).

Following Wise et al. (2012b), we adopt a Pop III IMF of the form:

$$f(\log M) dM = M^{-1.3} \exp \left[- \left(\frac{M_{\text{char}}}{M} \right)^{1.6} \right] dM \quad (1)$$

Above M_{char} , it behaves as a Salpeter IMF, and below M_{char} it is exponentially suppressed (Chabrier 2003). We also include an upper mass limit M_{max} . The Pop II IMF is sampled from a Kroupa (2001) distribution with a mass range of $0.08\text{--}120 M_\odot$.

All simulations include stellar feedback from stellar radiation and SNe:

- **Stellar Radiation:** Radiation in multiple bands (IR, FUV, LW, H I, He I, and He II) is tracked using adaptive ray-tracing radiative transfer methods.
- **SNe:** Core-collapse (both Pop III and Pop II) and Type Ia SNe inject mass, energy, and metals into the ISM with event-specific yields and energies.

We follow radiation from every star with mass $M > 8 M_\odot$. For Pop III stars, we use binned photon counts from Heger & Woosley (2010) with the lifetimes in Schaerer (2002). For Pop II stars, photon fluxes in each radiation band are determined using the OSTAR2002 (Lanz & Hubeny 2003) grid of O-type stellar models. We also use the PARSEC (Bressan et al. 2012) grid of stellar evolution tracks to set the lifetime of each Pop II star and the start time and length of the asymptotic giant branch (AGB) phase, if present.

All simulations employ a modified version of GRACKLE (Smith et al. 2017) to handle non-equilibrium chemistry involving nine species (H, H^+ , He, He^+ , He^{++} , e^- , H^- , H_2 , and H_2^+) and associated radiative cooling and heating processes. The chemical network includes dust-mediated H_2 formation, a UV background that extends to high redshift and is scaled to be continuous with Haardt & Madau (2012) at $z = 10$, and a Lyman-Werner background model from Emerick et al. (2019) and Wise et al. (2012b) that adopts updated rates at high redshift from Qin et al. (2020).

2.2. Differences Between Simulations

The two AEOS simulations (Aeos10 and Aeos20) differ in the characteristic mass M_{char} and upper limit M_{max} of their Pop III IMFs. The comparison simulations share the same Pop III IMF as Aeos10, but do not have star-by-star modeling for Pop II stars, do not model feedback from winds, and do not track detailed chemical enrichment with individual metals. These differences are summarized in Table 1.

Aeos10 adopts a Pop III IMF with a characteristic mass $M_{\text{char}} = 10 M_\odot$ and a maximum mass of $M_{\text{max}} = 100 M_\odot$. To investigate the sensitivity of galaxy evolution to the Pop III IMF, we execute an additional AEOS simulation (Aeos20) wherein the characteristic mass M_{char} of the Pop III IMF is modified from the fiducial value of $10 M_\odot$ to $20 M_\odot$ and $M_{\text{max}} = 300 M_\odot$ (motivated by Hirano & Bromm 2017; Bromm 2013; Yoshida 2006; Skinner & Wise 2020). This adjustment alters the mass distribution of Pop III stars, thereby affecting their lifetimes, feedback outputs, and chemical yields (see Brauer et al. 2025). This is the only difference between the Aeos10 and Aeos20 simulations.

In the AEOS simulations, Aeos10 and Aeos20, star particles represent individual stars sampled from their respective IMFs except for Pop II stars below $2 M_\odot$, which are aggregated into single particles due to their negligible feedback and enrichment contributions on simulation timescales. Star formation occurs from gas reservoirs of $\geq 100 M_\odot$.

Table 1. Overview of AEOS Simulation Runs

Run Name	Pop III M_{char}	Pop III M_{max}	Pop II Star Resolution	Individual Metals	Stellar Winds
Aeos10	10 M_{\odot}	100 M_{\odot}	2 M_{\odot}	Yes	Yes
Aeos20	20 M_{\odot}	300 M_{\odot}	2 M_{\odot}	Yes	Yes
Comparisons	10 M_{\odot}	100 M_{\odot}	1000 M_{\odot}	No	No

In the comparison simulations, Pop III stars are represented by individual particles, but Pop II stars are represented by star cluster particles with a minimum mass of 1000 M_{\odot} . For Pop II star formation, stars are formed from gas reservoirs of $\geq 1000 M_{\odot}$.

In addition to feedback from CCSNe and radiation, AEOS simulations include feedback and enrichment from AGB winds and massive star winds. The seven comparison simulations presented here omit AGB and massive stellar winds. They also omit individual star-by-star feedback modeling due to their aggregation of Pop II stars into cluster particles.

Additionally, the comparison simulations track overall metallicity but do not track individual elements. The AEOS simulations track the evolution of ten individual metal abundances – C, N, O, Na, Mg, Ca, Mn, Fe, Sr, and Ba – in addition to hydrogen and helium. These elements are sourced from various nucleosynthetic channels, including core-collapse SNe, Type Ia SNe, and asymptotic giant branch stars. We use detailed yield tables from Heger & Woosley (2010) for Pop III CCSNe and Limongi & Chieffi (2018) for Pop II stars.

3. EFFECTS OF VARYING POP III IMF

3.1. Ionization

The different Pop III IMFs in Aeos10 and Aeos20 lead to a pronounced difference in the hydrogen ionization of the simulation volume. Figure 1 shows that Aeos20 ionizes much more rapidly than Aeos10, with the volume 30% ionized by $z = 14.5$ in Aeos20 compared to 9% in Aeos10.

This occurs because the ionizing radiation emitted by a star increases with its mass (Schaerer 2002). Consequently, the IMF in Aeos20, with its higher M_{char} and upper mass limit, produces a stellar population that emits significantly more ionizing photons. Figure 2 shows the mass distribution of Pop III stars in the two simulations. Aeos10 contains approximately 2000 stars with masses in the tens of solar mass range, while Aeos20 has fewer than 500 stars in this range. However, Aeos20 features Pop III stars up to 300 M_{\odot} , including about 80 stars exceeding 100 M_{\odot} . The total number of ionizing photons from Pop III stars per stellar mass for these two distributions (combining the histograms and rate of ionizing photons shown in Figure 2) is about 7×10^{61} photons/ M_{\odot} for Aeos10 and 10×10^{61} photons/ M_{\odot} for Aeos20.

These massive stars are the primary contributors to the increased ionizing photon output, as shown in Figure 3. The

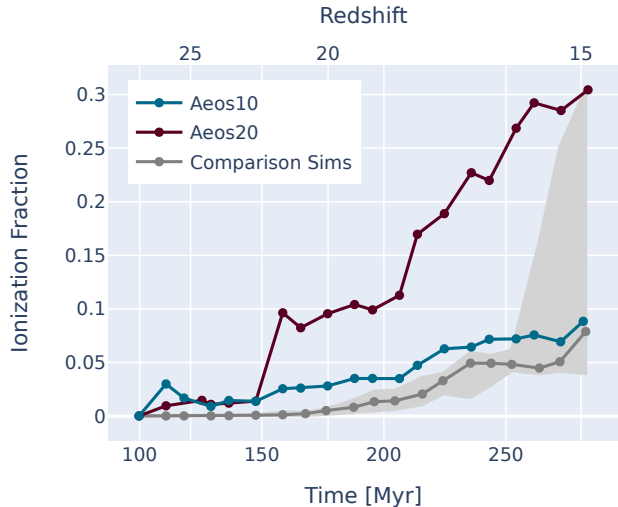


Figure 1. Ionization fraction of the simulation volume over time for Aeos10, Aeos20, and the comparison simulations using the Aeos10 Pop III IMF but without individual stellar feedback. The shaded grey region shows the 16th to 84th percentile of ionization fractions for the different comparison simulations. Aeos20 ionizes the volume significantly earlier than Aeos10 due to the more massive Pop III stars producing more ionizing photons. The comparison simulations have similar ionization to Aeos10, as expected, with stochastic differences beginning to cause large variations between simulations after around 250 Myr. The choice of Pop III IMF significantly affects the ionization and consequently the growth of the smallest galaxies.

total ionizing luminosity of Aeos20 surpasses Aeos10 due to its most massive stars. When only stars below 100 M_{\odot} are included, the total ionizing luminosity of Aeos20 agrees fairly well with that of Aeos10; the major peaks in ionizing luminosity are no longer seen. Thus, the enhanced ionization in Aeos20 seen in Figure 1 is predominantly driven by its population of Pop III stars exceeding 100 M_{\odot} .

The characteristic mass of the IMF also affects the ionization. If enhanced ionization was driven only by the most massive Pop III stars, we would expect the ionizing output from Aeos20 stars below 100 M_{\odot} to be significantly lower than in Aeos10, as we are excluding a substantial portion of stellar mass. However, since the total ionizing luminosity remains comparable to Aeos10, this indicates that the characteristic mass also contributes to ionizing luminosity, albeit to a lesser extent than the high-mass tail of the IMF. Additionally, in terms of total stellar mass, Aeos20 actually produces somewhat less stellar mass than Aeos10 at both early and

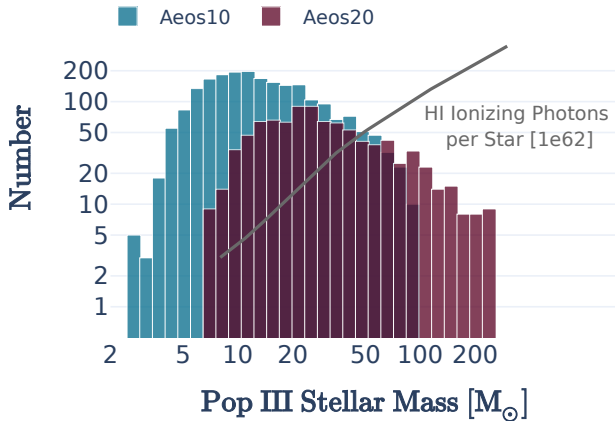


Figure 2. Distribution of Pop III star masses in Aeos10 vs. Aeos20. Aeos10 has far more low-mass Pop III stars, while Aeos20 has fewer total Pop III stars but their masses extend up to $300 M_{\odot}$. The black line shows the number of HI ionizing photons from each star as a function of stellar mass; several dozen Pop III stars with $> 100 M_{\odot}$ in Aeos20 result in a large number of ionizing photons.

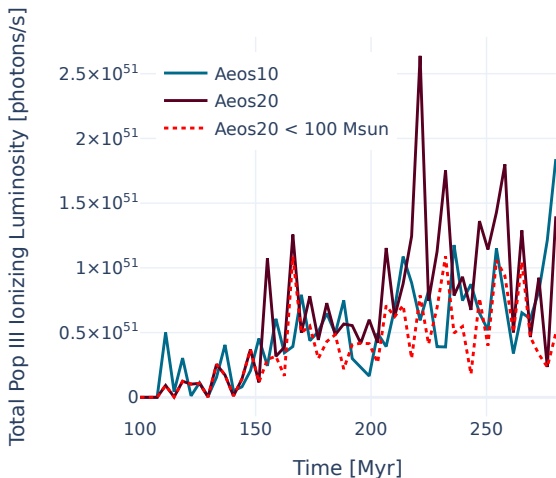


Figure 3. Starting after ~ 150 Myr, Aeos20 (maroon) begins to exceed Aeos10 (blue) in the total ionizing luminosity from Pop III stars. This excess of ionizing photons is primarily due to the luminosity of stars greater than $100 M_{\odot}$, because when the contribution of these stars is removed (dotted red), the total luminosity of the two simulations is far more similar.

late times, emphasizing that the higher ionization is due to the distribution of Pop III star masses rather than differences in total stellar mass.

The higher ionization in Aeos20 suppresses the formation of small galaxies. Previous work has found that ionization-driven photoheating of the gas in and around dwarf galaxies suppresses star formation (Efstathiou 1992; Bullock et al. 2000), particularly in halos with $M_{\text{halo}} \lesssim 10^9 M_{\odot}$ (e.g., Thoul & Weinberg 1996; Okamoto et al. 2008; Dawoodbhoy et al.

2018). In our simulations, all galaxies exist in small halos and we find they are highly sensitive to the rate of reionization. As seen in Figure 4, Aeos10 has far more galaxies at low halo masses. For $M_* < 100 M_{\odot}$, Aeos10 has 60 star-forming halos while Aeos20 has only 14 at $z = 14.5$. Meanwhile, the distributions of halo masses for all halos are essentially identical for Aeos10, Aeos20, and the comparison simulations, as expected for simulations with the same dark matter initialization. Another mechanism, Lyman-Werner (LW) radiation, can also suppress early star formation by dissociating H_2 , the primary coolant in metal-poor gas (e.g., Safranek-Shrader et al. 2012). Both Aeos10 and Aeos20 have identical LW backgrounds, however, so the suppression of small galaxy formation in Aeos20 vs. Aeos10 is isolated to the differences in ionizing photons.

We selected Aeos10 as our fiducial simulation in Brauer et al. (2025) because the high level of ionization in Aeos20 causes reionization to occur much earlier than expected: 30% ionized at redshift $z \sim 14$ compared to the inferred redshift of $z \sim 8$ from Planck Collaboration et al. (2016). Our simulation volume is a small region that is not generally representative of the very early Universe, however. We thus avoid interpreting this early reionization as a constraint on the Pop III IMF, which remains highly uncertain. Instead, we interpret the differences between Aeos10 and Aeos20 as evidence of the strong impact that different Pop III IMF choices have on reionization and the number of small, early galaxies. Given both the importance of the Pop III IMF and its uncertainty, simulations of the first galaxies must take care to understand the impact of Pop III IMF choices on their results.

3.2. Chemical Enrichment

Nucleosynthetic yields from Pop III core-collapse SNe depend on their masses (Heger & Woosley 2010). These yields differ not only in total metal production but also in the relative abundances of individual metals (Rossi et al. 2024; Brauer et al. 2025).

When we vary the Pop III IMF, we thus produce different chemical abundances in the subsequent Pop II stars. In Figure 5, we show how the differences in yields translate into the chemical abundances of the oldest Pop II stars. We show the median stellar chemical abundances of first-generation Pop II stars from each galaxy in the simulations that has begun Pop II star formation (17 galaxies in Aeos10, 15 galaxies in Aeos20). We limit the analysis to low-mass stars, as more massive stars would not survive to the present-day.

While stellar chemical abundance differences are apparent in the Figure, we note that the halo-to-halo scatter is significant for some of the elements as shown by the scatter bars. To quantify the number of Pop II halos required to distinguish differences resulting from these Pop III IMFs, we estimate the sample size necessary for the mean abundances

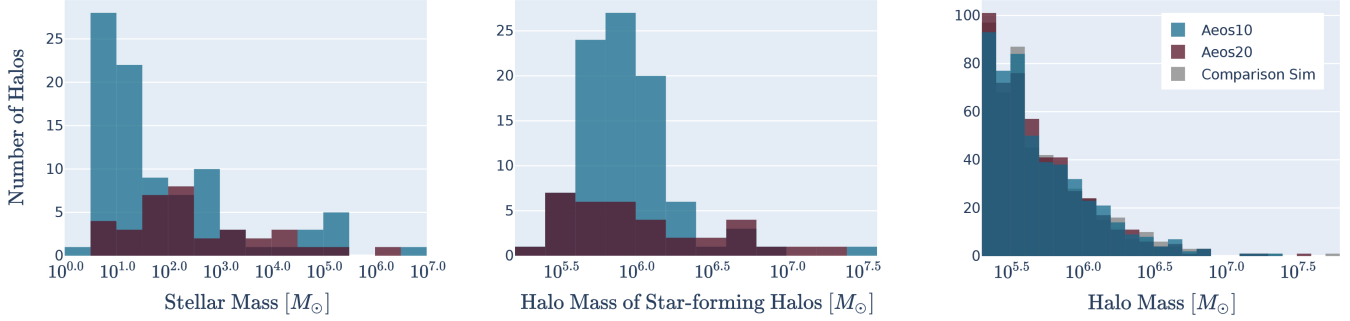


Figure 4. Stellar masses and halo masses of star-forming halos in the different simulations. (a) Comparing the star-forming halos in Aeos10 vs. Aeos20. Aeos10 has many more small star-forming halos than Aeos20. This is due to higher ionization in Aeos20 (see Figure 1). The distribution of halo masses for all halos in all simulations are nearly identical, as expected.

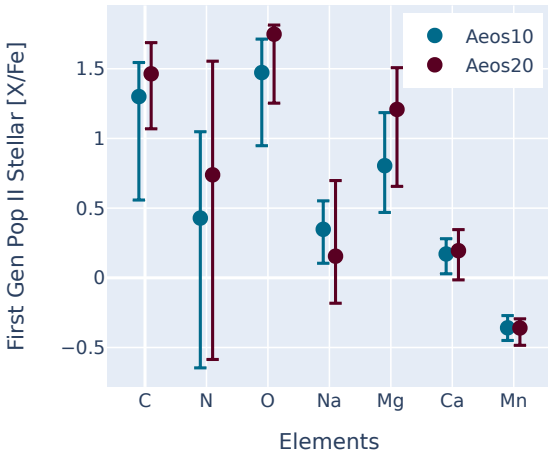


Figure 5. Median stellar chemical abundances ($[X/Fe]$) of the oldest low-mass Pop II stars from each halo that has started Pop II star formation in the simulation with 16th to 84th percentile scatter between the different halos. The mass of Pop III stars affects their yields, affecting the abundances in first generation Pop II stars. In particular, light elements (C, N) and α -elements (O, Mg) are increased in the yields of higher-mass Pop III stars, and elements with even atomic numbers (e.g., Mg) are more abundant relative to odd-numbered elements (e.g., Na). The scatter between halos is significant compared to the differences due to adopted Pop III IMF, however.

to separate beyond the intrinsic halo-to-halo scatter. For elements such as C and N, more than 20–30 halos are needed to achieve statistical significance, while elements such as Mg and O require fewer than 10. Given the current sample of 15–17 Pop II halos per simulation, this suggests that stochastic enrichment dominates over systematic trends for several elements, emphasizing the need for larger sample sizes when interpreting the impact of Pop III IMF variations on early chemical enrichment.

Pop II stars in Aeos20 exhibit higher $[X/Fe]$ values for light elements such as nitrogen (N) and oxygen (O), reflecting the increased nucleosynthetic yields from more massive Pop III

stars due to stronger α -capture reactions and rotational mixing (Heger & Woosley 2010). Carbon (C) is also enhanced in Aeos20, primarily due to the significant production of carbon during helium burning in more massive Pop III stars. In these simulations we do not include pair-instability SNe (Rakavy & Shaviv 1967; Fraley 1968; Woosley et al. 2002), which may occur for high-mass ($\gtrsim 140 M_{\odot}$) Pop III stars (e.g. Schneider et al. 2004; Takahashi et al. 2016; de Bannasuti et al. 2017), but this would further enhance the amount of carbon due to their efficient ejection of carbon-rich material. For α -elements such as magnesium (Mg), silicon (Si), and calcium (Ca), Aeos20 also tends to show higher $[X/Fe]$ ratios, consistent with the Heger & Woosley (2010) yields and the expectation that more massive Pop III stars are more efficient producers of α -elements during their evolution and subsequent SN explosions.

Figure 5 also demonstrates an enhanced odd-even effect, where odd-Z elements such as sodium (Na) and manganese (Mn) are produced in lower relative abundances compared to their even-Z counterparts (e.g., Mg, Ca). This effect is generally more pronounced in Aeos20, as the larger number of very massive stars amplifies the odd-even disparity due to differences in nuclear reaction rates. The scatter, shown by the error bars, indicates significant halo-to-halo variation with tighter distributions for certain elements like Mn and Ca, suggesting a more uniform enrichment pattern in these elements in comparison to Fe. These results underscore how the initial mass function of Pop III stars strongly influences the chemical abundance patterns of their direct Pop II descendants, shaping both light and α -element production as well as odd-even abundance ratios.

The enhanced carbon yield of more massive Pop III stars results in different amounts of carbon-enhanced metal-poor (CEMP) stars. CEMP stars, identified by their high carbon-to-iron ratios (taken either at $[C/Fe] > 0.7$ or $[C/Fe] > 1.0$), provide key insights into the formation of the first stars and galaxies (Beers & Christlieb 2005; Jeon et al. 2017). Fig-

Figure 6 shows the cumulative fractions of our simulated CEMP stars as a function of metallicity. Because more massive Pop III stars produce a higher ratio of carbon to iron, Aeos20 has a higher fraction of CEMP stars than Aeos10. While they reproduce the qualitative trends, compared with the observed fractions of CEMP stars in the Milky Way (Placco et al. 2014; Yoon et al. 2018), neither Aeos10 nor Aeos20 overproduce CEMP stars at a given $[\text{Fe}/\text{H}]$. Generally, at the lowest metallicities that are most sensitive to Pop III enrichment, Aeos10 stars have lower fractions than observations and Aeos20 stars have higher fractions. This shows that the differences in Pop III initial mass functions between Aeos10 and Aeos20 significantly affect CEMP fractions and therefore points toward an improved IMF that can better reproduce Milky Way observations.

However, at the same time, there are inconsistencies in the fractions of carbon-enhanced metal-poor stars between different Milky Way stellar surveys (Arentsen et al. 2022; Ardern-Arentsen et al. 2025). Observations of dwarf galaxies also tend to find lower fractions of CEMP stars as compared to the Milky Way (e.g., Chiti et al. 2018; Sestito et al. 2024; Ou et al. 2025, Yelland et al. in prep). Furthermore, Pop III SNe likely exhibited a range of explosion energies (Kobayashi et al. 2006; Heger et al. 2003) that affected the metal retention of early galaxies (Cooke & Madau 2014; Rossi et al. 2024). Our current simulations do not capture the effects of different explosion energies. Additional low-metallicity observations and simulations of larger boxes with a broader range of IMF variations and Pop III SNe explosion energies to further explore these discrepancies.

While there are differences in the enrichment of individual metals, the differences in Pop III IMF do not produce a noticeable difference in the stellar mass-metallicity relationships of the Aeos10 and Aeos20 simulations, as seen in Figure 7. This may be because the increased metal yields from more massive Pop III stars in Aeos20 are counterbalanced by their lower metal ejection efficiency. As modeled by Heger & Woosley (2010), massive Pop III stars often undergo fallback SNe, where a portion of the metals produced in the core region falls back onto the nascent black hole. This resulting metal retention depends on the explosion energy and stellar mass, and reduces the metals ejected into the interstellar medium and potentially limits the overall enrichment effect of these stars. Since we use the yields of Heger & Woosley (2010), our results inherently reflect this mechanism. Additionally, many of the more massive halos in our models have begun forming Pop II stars, which quickly dominate their hosts' enrichment, obscuring differences from Pop III enrichment. To study the impact of different Pop III IMFs on chemical enrichment, it is therefore essential to focus exclusively on the oldest Pop II stars.

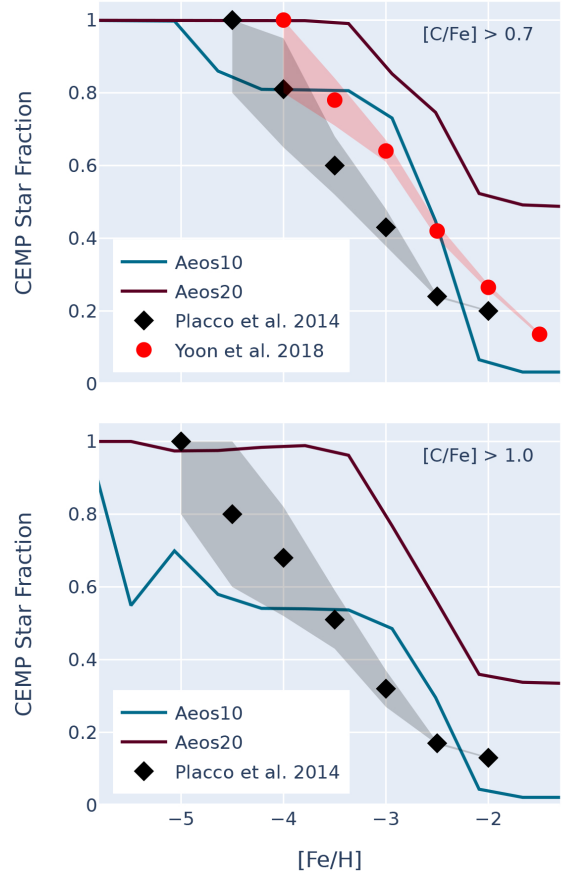


Figure 6. Cumulative fractions of carbon-enhanced metal-poor (CEMP) stars as a function of metallicity. Top panel shows CEMP stars with $[\text{C}/\text{Fe}] > 0.7$ and bottom panel shows CEMP stars with $[\text{C}/\text{Fe}] > 1.0$. The low-mass Aeos10 stars are shown as a teal line, the low-mass Aeos20 stars are shown as a maroon line, observations from Placco et al. (2014) are shown as diamonds, and observations from Yoon et al. (2018) are shown as circles. The Pop III IMF significantly affects the fraction of CEMP stars, and neither of the Aeos10 nor Aeos20 IMFs reproduce Milky Way observations.

In observations, the very faintest dwarf galaxies appear to exhibit a metallicity floor rather than further extending the mass-metallicity relationship found for the more luminous galaxies (e.g., Ahvazi et al. 2024; Heiger et al. 2024). Across three orders of magnitude in luminosity ($10^2 - 10^5 M_{\odot}$), ultra-faint dwarf galaxies show a nearly constant mean metallicity, scattered around $[\text{Fe}/\text{H}] \sim -2.6$ (Fu et al. 2023). This contrasts with the expectation that less massive galaxies should have lower average metallicities. The observed plateau is not yet fully understood, but may be caused by Pop III enrichment (Wheeler et al. 2019), a ceiling on mass outflows (Kravtsov & Manwadkar 2022), or the possibility that these galaxies were once more massive and later lost stellar mass due to tidal disruption (e.g., Kirby et al. 2013). In the AEOS simulations, we find that Pop III enrichment results in

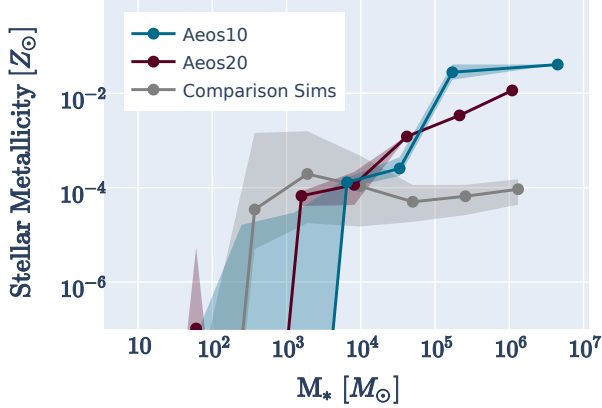


Figure 7. Mass-metallicity relation for galaxies in Aeos10, Aeos20, and the comparison simulations at $z = 14.5$. The shaded regions represent 16th to 84th percentile scatter.

a median metallicity floor of approximately $Z = 10^{-4} Z_{\odot}$ (see also Figure 8 of Brauer et al. 2025) with increasing stellar metallicities for galaxies of $\sim 10^5 M_{\odot}$ and greater. This is a slightly lower metallicity floor than seen in observed dwarf galaxies, implying either additional Pop III enrichment in observed galaxies or that an additional mechanism is necessary.

4. COMPARISON TO SIMULATIONS WITHOUT INDIVIDUAL STELLAR FEEDBACK

To better understand the implications of modeling individual stars and run-to-run variations, we also ran seven comparison simulations without individual Pop II star particles, without individual stellar feedback, and without detailed metal tracing. Otherwise, these simulations have the same initial conditions, cosmological parameters, and Pop III IMF as Aeos10.

Pop III stars are represented as individual particles in all simulations. However, the comparison simulations resolve Pop II stars as cluster particles of $\sim 1000 M_{\odot}$, as in Skinner & Wise (2020), while Aeos10 and Aeos20 resolve every Pop II star with $M > 2 M_{\odot}$ as an individual particle.

The cumulative Pop III and Pop II star formation of the comparison simulations can be seen in the top panel of Figure 8. While differences exist in the overall star formation history, the differences are similar in magnitude to stochastic differences seen between identically initialized simulations, with the exception that Pop II formation tends to begin slightly earlier in the comparison simulations. However, the difference in onset of Pop II star formation is not large, and could be due to stochastic differences. As seen in the bottom of Figure 8, Aeos10 and the comparison simulations do not significantly differ in their overall star formation history. Aeos10 and Aeos20 also resemble each other, though Aeos20 starts star formation slightly behind Aeos10. In general, the bulk properties of total star formation and stellar

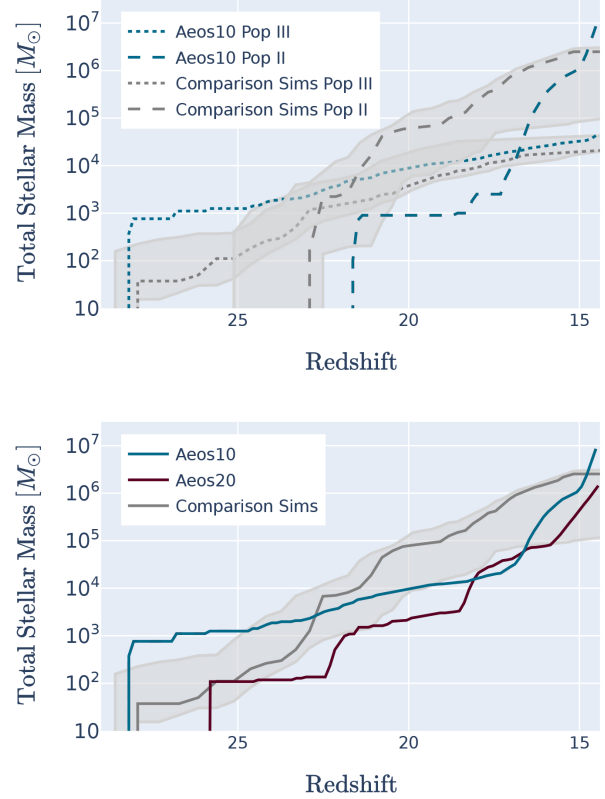


Figure 8. Cumulative star formation history of the full domain down to redshift $z = 14.5$. Top: Pop III and Pop II star formation of the Aeos10 volume as compared to the star formation of the comparison simulations (without individual Pop II star particles or individual feedback). The shaded gray regions show 16th to 84th percentile scatter between all comparison simulations. Bottom: Total cumulative star formation for Aeos10, Aeos20, and the comparison simulations. These bulk properties of the galaxies are not significantly affected by the inclusion of individual stars and stellar feedback.

mass-halo mass relation are not highly affected by the differences between the AEOS simulations and the comparison simulations.

Figure 9 shows the mass distribution of star-forming halos in Aeos10 vs. a comparison simulation. As expected, when looking only at halo mass, the distributions are similar; the halo mass is dominated by dark matter, which does not differ between the simulations. The stellar masses, however, differ. The comparison simulations have a tendency to form galaxies of at least a few thousand solar masses because the Pop II star particles form in masses of $\sim 1000 M_{\odot}$. The number of Pop II halos in each comparison simulation differs from just a few to a few dozen, but in aggregate, there is a trend towards more galaxies around $1000 M_{\odot}$ than in the AEOS simulations. The AEOS galaxies, on the other hand, can include Pop II galaxies with stellar masses as low as a few tens of solar masses (see Brauer et al. 2025). Additionally, both

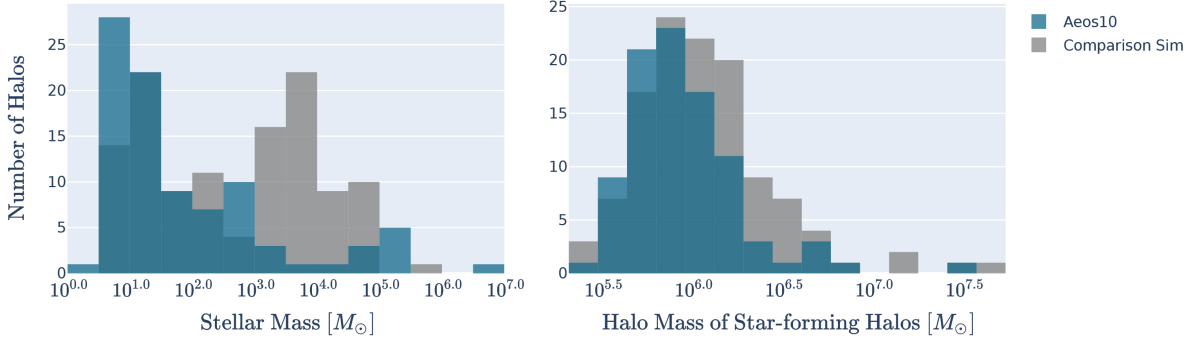


Figure 9. Comparing the star-forming halos in Aeos10 with those in a typical comparison simulation. The stellar mass distributions differ; the comparison simulations generally form more galaxies around $\sim 1000 M_{\odot}$. This is because in the comparison simulations, the Pop II stars form in particles of $1000 M_{\odot}$, biasing any halo that has begun Pop II star formation to contain at least $1000 M_{\odot}$. The halo mass distributions are more similar because the dark matter modeling is the same between simulations.

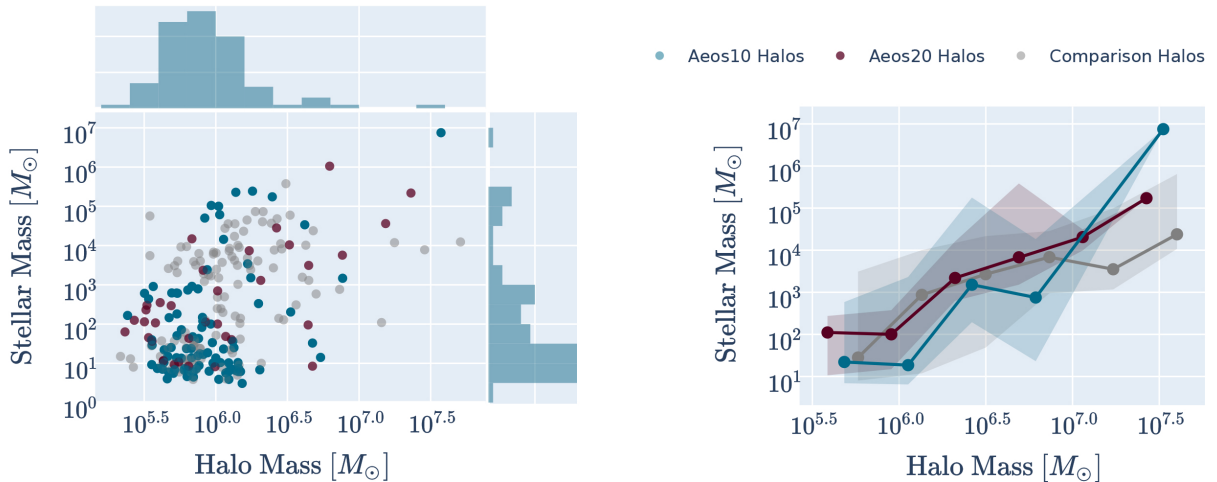


Figure 10. Left: Individual stellar masses and halo masses of every star-forming halo in the simulations at redshift $z = 14.5$. Shown are the halos from Aeos10, Aeos20, and a typical comparison simulation. Aeos10 is also shown in the histograms (see Figures 4 and 9 for the histograms of Aeos20 and comparison simulations). Right: Mean stellar-mass to halo-mass relation with scatter for the different simulations, summarizing the body of simulated data on the left.

the AEOS simulations and comparison simulations can have stripped stars, resulting in the peak at a few M_{\odot} .

When looking at the overall $M_{*} - M_{\text{halo}}$ relations of the different simulations in Figure 10, however, there is not a large difference. This is largely because the scatter in the relation within a given simulation (due both to stochastic differences between comparison simulations and scatter in halos within each simulation) is just as significant as the differences between simulations. For halos greater than $\gtrsim 10^7 M_{\odot}$, the AEOS simulations start to form galaxies with more stellar mass than the comparison simulations. This suffers from small number statistics, though. The comparison simulations also are forced towards Pop II galaxies of at least $1000 M_{\odot}$, as previously discussed.

The metallicities of the galaxies in the comparison simulations differ more significantly from those of the AEOS galax-

ies. Figure 7 shows the median mass-metallicity relation for each simulation with 16% to 84% scatter. The comparison simulations have a much shallower mass-metallicity relation than the AEOS simulations. The AEOS simulations have a log-log slope of ~ 1 , which is steeper than the typical ~ 0.3 slope of other simulated mass-metallicity relations (Collins & Read 2022), and much steeper than the practically flat relation of all the comparison simulations. The steeper AEOS slope in contrast to the slope of the comparison simulations may be due in part to the star-by-star modeling. Both our previous work and other star-by-star simulations (Brauer et al. 2025; Jeon & Ko 2024; Andersson et al. 2025) have found that the relatively weaker feedback of the star-by-star method (compared to burstier, stronger feedback from traditional single stellar populations) leads to the possibility of higher stellar masses at a given halo mass – we start to see this in the

stellar masses of our most massive galaxies, and likely do not see it at lower stellar masses in part due to the stellar mass resolution of the comparison simulations. This relatively weaker feedback could also allow greater retention of metals, and thus a steeper mass-metallicity relation as seen in Figure 7. In the comparison simulations, the aggregated bursty feedback from the more massive cluster particles (which quickly dominate galaxies with $M_* > 10^3 M_\odot$) appear to eject metals more efficiently, reducing the expected increase in metallicity in halos between $10^3 M_\odot$ and $10^6 M_\odot$ in stellar mass. These halos are generally still low in total mass and have high loss fractions, making them highly sensitive to increases in feedback (see also Mead et al. 2025). We note, though, that the slope at higher halo mass is based on very few galaxies and the slope at lower halo mass is dominated by scatter. In particular, the difference in the largest galaxy and the metallicity of its surrounding galaxies between Aeos10 and the comparison galaxies is mostly due to a single burst of Pop II formation that occurs at the end of the Aeos10 run, so we refrain from drawing conclusions about $M_* > 10^5 M_\odot$ galaxies until longer-running simulations have been completed.

In summary, most bulk properties do not significantly differ between Aeos10 and the comparison simulations. One difference is that the comparison simulations are unable to properly form Pop II galaxies below the aggregated star particle resolution, resulting in a tendency to form more galaxies around the resolution limit. The inclusion of individual Pop II stellar feedback also tends to result in less bursty, overall weaker feedback in comparison to traditional single stellar populations, allowing for greater accumulation of metals and stellar mass.

5. CONCLUSIONS

Our analysis of the AEOS simulations (Brauer et al. 2025) shows how varying the Pop III IMF and implementing a star-by-star feedback model influence early galaxy formation and evolution. We run two simulations with different Pop III IMFs: Aeos10, with a characteristic Pop III mass of $10 M_\odot$ and an upper cutoff of $100 M_\odot$, and Aeos20, with a characteristic Pop III mass of $20 M_\odot$ and an upper cutoff of $300 M_\odot$. By comparing the Aeos10 and Aeos20 simulations, we demonstrate that variations in the Pop III IMF significantly affect the ionization history, the number of early galaxies, and the chemical abundance patterns in subsequent Pop II stars. Aeos20, with its more massive Pop III stars, produces more ionizing photons, leading to substantially earlier ionization and consequently a suppression of small galaxy formation compared to what is occurring in Aeos10.

The chemical enrichment of Aeos10 and Aeos20 differ, especially in first-generation Pop II stars. In Aeos20, the more massive Pop III stars produce yields with enhanced amounts of light elements and α -elements. The more massive Pop III

stars also produce yields with an enhanced odd-even effect, increasing the amount of elements with even atomic numbers (e.g., Mg) relative to odd-numbered elements (e.g., Na). This is reflected in the stellar chemical abundances of the first-generation Pop II stars. Aeos20 also produces a greater fraction of CEMP stars, showing that CEMP stars provide important insights into the properties of the first stars. The scatter in chemical abundances between Pop II stars from different galaxies is high though, especially in light elements, and dominates many of the differences resulting from the Pop III IMF.

We also run a suite of comparison simulations that lack individual star modeling. Comparisons with these simulations reveal that the high stellar resolution and star-by-star feedback in AEOS create differences in the stellar mass distribution and the mass-metallicity relation. While Pop II star formation is still relatively new, the comparison simulations tend to form more galaxies approximately around the mass of their Pop II aggregate star particle resolution, $1000 M_\odot$, while the AEOS simulations avoid this by allowing Pop II stars to form from less massive gas reservoirs. Additionally, the star-by-star approach tends to result in galaxies with comparatively more stellar mass, as explored by Jeon & Ko (2024); Andersson et al. (2025); Brauer et al. (2025), due at least in part to less bursty feedback. This enables a greater accumulation of metals after Pop II star formation begins and consequently steeper mass-metallicity relations compared to simulations that represent stellar populations as single particles.

Despite these differences, most of the bulk properties, such as the total star formation history, remain fairly consistent across all simulations. This highlights the robustness of certain galaxy formation trends while emphasizing the sensitivity of small-scale processes to detailed modeling choices.

Ultimately, this work underscores the importance of carefully considering the Pop III IMF and feedback resolution in simulations of early galaxy formation. As uncertainties in the Pop III IMF persist, future studies must explore the interplay of these parameters to refine our understanding of the first galaxies and their role in cosmic reionization. Further observational data on metal-poor stars and additional simulations extending to later epochs will provide constraints on these early processes.

ACKNOWLEDGMENTS

K.B. is supported by an NSF Astronomy and Astrophysics Postdoctoral Fellowship under award AST-2303858. J.M. acknowledges support from the NSF Graduate Research Fellowship under grant DGE-2036197. J.H.W. acknowledges support by NSF grant AST-2108020 and NASA grants 80NSSC20K0520 and 80NSSC21K1053. M.-M.M.L. and E.P.A. were partly supported by NSF grant AST-2307950

and NASA Astrophysical Theory grant 80NSSC24K0935. G.L.B. acknowledges support from the NSF (AST-2108470 and AST-2307419, ACCESS), a NASA TCAN award, and the Simons Foundation through the Learning the Universe Collaboration. A.P.J. acknowledges support from NSF grant AST-2307599. A.F. acknowledges support from NSF grant AST-2307436.

The authors acknowledge the Texas Advanced Computing Center at The University of Texas at Austin for providing HPC and storage resources under project AST20007, which supported the research presented in this paper.

REFERENCES

- Abel, T., Bryan, G. L., & Norman, M. L. 2002, *Science*, 295, 93
- Ahvazi, N., Benson, A., Sales, L. V., et al. 2024, *MNRAS*, 529, 3387
- Andersson, E. P., Agertz, O., Renaud, F., & Teyssier, R. 2023, *MNRAS*, 521, 2196
- Andersson, E. P., Rey, M. P., Pontzen, A., et al. 2025, *ApJ*, 978, 129
- Ardern-Arentsen, A., Kane, S. G., Belokurov, V., et al. 2025, *MNRAS*, 537, 1984
- Arentsen, A., Placco, V. M., Lee, Y. S., et al. 2022, *MNRAS*, 515, 4082
- Barkana, R., & Loeb, A. 2001, *PhR*, 349, 125
- Beers, T. C., & Christlieb, N. 2005, *ARA&A*, 43, 531
- Brauer, K., Ji, A. P., Frebel, A., et al. 2019, *ApJ*, 871, 247
- Brauer, K., Emerick, A., Mead, J., et al. 2025, *ApJ*, 980, 41
- Bressan, A., Marigo, P., Girardi, L., et al. 2012, *MNRAS*, 427, 127
- Bromm, V. 2013, *Reports on Progress in Physics*, 76, 112901
- Bromm, V., Coppi, P. S., & Larson, R. B. 2002, *ApJ*, 564, 23
- Brummel-Smith, C., Bryan, G., Butsky, I., et al. 2019, *The Journal of Open Source Software*, 4, 1636
- Bryan, G. L., Norman, M. L., O’Shea, B. W., et al. 2014, *ApJS*, 211, 19
- Bullock, J. S., Kravtsov, A. V., & Weinberg, D. H. 2000, *ApJ*, 539, 517
- Calura, F., Lupi, A., Rosdahl, J., et al. 2022, *MNRAS*, 516, 5914
- Chabrier, G. 2003, *PASP*, 115, 763
- Chiaki, G., Marassi, S., Nozawa, T., et al. 2015, *MNRAS*, 446, 2659
- Chiti, A., Simon, J. D., Frebel, A., et al. 2018, *ApJ*, 856, 142
- Collins, M. L. M., & Read, J. I. 2022, *Nature Astronomy*, 6, 647
- Cooke, R. J., & Madau, P. 2014, *ApJ*, 791, 116
- Dawoodbhoj, T., Shapiro, P. R., Ocvirk, P., et al. 2018, *MNRAS*, 480, 1740
- de Bressan, M., Salvadori, S., Schneider, R., Valiante, R., & Omukai, K. 2017, *MNRAS*, 465, 926
- Deng, Y., Li, H., Liu, B., et al. 2024, *arXiv e-prints*, arXiv:2405.08869
- Efstathiou, G. 1992, *MNRAS*, 256, 43P
- Emerick, A., Bryan, G. L., & Mac Low, M.-M. 2019, *MNRAS*, 482, 1304
- Fraley, G. S. 1968, *Ap&SS*, 2, 96
- Fraser, M., Casey, A. R., Gilmore, G., Heger, A., & Chan, C. 2017, *MNRAS*, 468, 418
- Fu, S. W., Weisz, D. R., Starkenburg, E., et al. 2023, *ApJ*, 958, 167
- Gutcke, T. A., Pakmor, R., Naab, T., & Springel, V. 2021, *MNRAS*, 501, 5597
- Haardt, F., & Madau, P. 2012, *ApJ*, 746, 125
- Hahn, O., & Abel, T. 2011, *MNRAS*, 415, 2101
- Hartwig, T., Bromm, V., Klessen, R. S., & Glover, S. C. O. 2015, *MNRAS*, 447, 3892
- Hartwig, T., Yoshida, N., Magg, M., et al. 2018, *MNRAS*, 478, 1795
- Heger, A., Fryer, C. L., Woosley, S. E., Langer, N., & Hartmann, D. H. 2003, *ApJ*, 591, 288
- Heger, A., & Woosley, S. E. 2010, *ApJ*, 724, 341
- Heiger, M. E., Li, T. S., Pace, A. B., et al. 2024, *ApJ*, 961, 234
- Hirai, Y., Fujii, M. S., & Saitoh, T. R. 2021, *PASJ*, 73, 1036
- Hirai, Y., Saitoh, T. R., Fujii, M. S., Kaneko, K., & Beers, T. C. 2024, *arXiv e-prints*, arXiv:2411.18680
- Hirano, S., & Bromm, V. 2017, *MNRAS*, 470, 898
- Hirano, S., Hosokawa, T., Yoshida, N., et al. 2014, *ApJ*, 781, 60
- Hislop, J. M., Naab, T., Steinwandel, U. P., et al. 2022, *MNRAS*, 509, 5938
- Hosokawa, T., Omukai, K., Yoshida, N., & Yorke, H. W. 2011, *Science*, 334, 1250
- Ishigaki, M. N., Tominaga, N., Kobayashi, C., & Nomoto, K. 2018, *ApJ*, 857, 46
- Jeon, M., Besla, G., & Bromm, V. 2017, *ApJ*, 848, 85
- Jeon, M., & Ko, M. 2024, *arXiv e-prints*, arXiv:2411.17862
- Ji, A. P., Frebel, A., & Bromm, V. 2014, *ApJ*, 782, 95
- Ji, A. P., Curtis, S., Storm, N., et al. 2024, *ApJL*, 961, L41
- Kimm, T., Katz, H., Haehnelt, M., et al. 2017, *MNRAS*, 466, 4826
- Kirby, E., Boylan-Kolchin, M., Cohen, J. G., et al. 2013, in *Probes of Dark Matter on Galaxy Scales*, Vol. 1, 40202
- Klessen, R. S., & Glover, S. C. O. 2023, *ARA&A*, 61, 65
- Kobayashi, C., Umeda, H., Nomoto, K., Tominaga, N., & Ohkubo, T. 2006, *ApJ*, 653, 1145
- Kravtsov, A., & Manwadkar, V. 2022, *MNRAS*, 514, 2667
- Kroupa, P. 2001, *MNRAS*, 322, 231
- Kulkarni, M., Visbal, E., & Bryan, G. L. 2021, *ApJ*, 917, 40

- Lahén, N., Naab, T., Johansson, P. H., et al. 2020, *ApJ*, 891, 2
- Lanz, T., & Hubeny, I. 2003, *ApJS*, 146, 417
- Lazar, A., & Bromm, V. 2022, *MNRAS*, 511, 2505
- Limongi, M., & Chieffi, A. 2018, *ApJS*, 237, 13
- Mead, J., Brauer, K., Bryan, G. L., et al. 2025, *ApJ*, 980, 62
- Okamoto, T., Gao, L., & Theuns, T. 2008, *MNRAS*, 390, 920
- Ou, X., Yelland, A., Chiti, A., et al. 2025, *arXiv e-prints*, [arXiv:2501.14061](https://arxiv.org/abs/2501.14061)
- Parsons, J., Mas-Ribas, L., Sun, G., et al. 2022, *ApJ*, 933, 141
- Placco, V. M., Frebel, A., Beers, T. C., & Stancliffe, R. J. 2014, *ApJ*, 797, 21
- Planck Collaboration, Ade, P. A. R., Aghanim, N., et al. 2014, *A&A*, 571, A16
- Planck Collaboration, Adam, R., Aghanim, N., et al. 2016, *A&A*, 596, A108
- Prgomet, M., Rey, M. P., Andersson, E. P., et al. 2022, *MNRAS*, 513, 2326
- Qin, Y., Mesinger, A., Park, J., Greig, B., & Muñoz, J. B. 2020, *MNRAS*, 495, 123
- Rakavy, G., & Shaviv, G. 1967, *ApJ*, 148, 803
- Rossi, M., Salvadori, S., & Skúladóttir, Á. 2021, *MNRAS*, 503, 6026
- Rossi, M., Salvadori, S., Skúladóttir, Á., Vanni, I., & Koutsouridou, I. 2024, *arXiv e-prints*, [arXiv:2406.12960](https://arxiv.org/abs/2406.12960)
- Safranek-Shrader, C., Agarwal, M., Federrath, C., et al. 2012, *MNRAS*, 426, 1159
- Schaerer, D. 2002, *A&A*, 382, 28
- Schneider, R., Ferrara, A., & Salvaterra, R. 2004, *MNRAS*, 351, 1379
- Schneider, R., Omukai, K., Bianchi, S., & Valiante, R. 2012, *MNRAS*, 419, 1566
- Schneider, R., Salvaterra, R., Ferrara, A., & Ciardi, B. 2006, *MNRAS*, 369, 825
- Sestito, F., Ardern-Arentsen, A., Vitali, S., et al. 2024, *A&A*, 690, A333
- Skinner, D., & Wise, J. H. 2020, *MNRAS*, 492, 4386
- Skúladóttir, Á., Koutsouridou, I., Vanni, I., et al. 2024, *ApJL*, 968, L23
- Smith, B. D., Bryan, G. L., Glover, S. C. O., et al. 2017, *MNRAS*, 466, 2217
- Smith, M. C. 2021, *MNRAS*, 502, 5417
- Somerville, R. S., & Davé, R. 2015, *ARA&A*, 53, 51
- Stacy, A., Bromm, V., & Lee, A. T. 2016, *MNRAS*, 462, 1307
- Steinwandel, U. P., Bryan, G. L., Somerville, R. S., Hayward, C. C., & Burkart, B. 2023, *MNRAS*, 526, 1408
- Susa, H., Hasegawa, K., & Tominaga, N. 2014, *ApJ*, 792, 32
- Takahashi, K., Yoshida, T., Umeda, H., Sumiyoshi, K., & Yamada, S. 2016, *MNRAS*, 456, 1320
- Thoul, A. A., & Weinberg, D. H. 1996, *ApJ*, 465, 608
- Tumlinson, J. 2006, *ApJ*, 641, 1
- Wheeler, C., Hopkins, P. F., Pace, A. B., et al. 2019, *MNRAS*, 490, 4447
- Wise, J. H., & Abel, T. 2008, *ApJ*, 685, 40
- Wise, J. H., Abel, T., Turk, M. J., Norman, M. L., & Smith, B. D. 2012a, *MNRAS*, 427, 311
- Wise, J. H., Turk, M. J., Norman, M. L., & Abel, T. 2012b, *ApJ*, 745, 50
- Woosley, S. E., Heger, A., & Weaver, T. A. 2002, *Reviews of Modern Physics*, 74, 1015
- Xing, Q.-F., Zhao, G., Liu, Z.-W., et al. 2023, *Nature*, 618, 712
- Yoon, J., Beers, T. C., Dietz, S., et al. 2018, *ApJ*, 861, 146
- Yoshida, N. 2006, *NewAR*, 50, 19